Lab on a Chip

PAPER

Gas–liquid–liquid three-phase flow pattern and pressure drop in a microfluidic chip: similarities with gas–liquid/liquid–liquid flows†

Cite this: *Lab Chip*, 2014, **14**, 1632

Jun Yue,[a] Evgeny V. Rebrov[b] and Jaap C. Schouten*[a]

We report a three-phase slug flow and a parallel-slug flow as two major flow patterns found under the nitrogen–decane–water flow through a glass microfluidic chip which features a long microchannel with a hydraulic diameter of 98 μm connected to a cross-flow mixer. The three-phase slug flow pattern is characterized by a flow of decane droplets containing single elongated nitrogen bubbles, which are separated by water slugs. This flow pattern was observed at a superficial velocity of decane (in the range of about 0.6 to 10 mm s^{-1}) typically lower than that of water for a given superficial gas velocity in the range of 30 to 91 mm s^{-1}. The parallel-slug flow pattern is characterized by a continuous water flow in one part of the channel cross section and a parallel flow of decane with dispersed nitrogen bubbles in the adjacent part of the channel cross section, which was observed at a superficial velocity of decane (in the range of about 2.5 to 40 mm s^{-1}) typically higher than that of water for each given superficial gas velocity. The three-phase slug flow can be seen as a superimposition of both decane–water and nitrogen–decane slug flows observed in the chip when the flow of the third phase (*viz*. nitrogen or water, respectively) was set at zero. The parallel-slug flow can be seen as a superimposition of the decane–water parallel flow and the nitrogen–decane slug flow observed in the chip under the corresponding two-phase flow conditions. In case of small capillary numbers (Ca ≪ 0.1) and Weber numbers (We ≪ 1), the developed two-phase pressure drop model under a slug flow has been extended to obtain a three-phase slug flow model in which the 'nitrogen-in-decane' droplet is assumed as a pseudo-homogeneous droplet with an effective viscosity. The parallel flow and slug flow pressure drop models have been combined to obtain a parallel-slug flow model. The obtained models describe the experimental pressure drop with standard deviations of 8% and 12% for the three-phase slug flow and parallel-slug flow, respectively. An example is given to illustrate the model uses in designing bifurcated microchannels that split the three-phase slug flow for high-throughput processing.

Received 26th November 2013,
Accepted 10th February 2014

DOI: 10.1039/c3lc51307f

www.rsc.org/loc

Introduction

Multiphase flow in microfluidic chips has attracted a large amount of research interest over the past decade because of its promising uses in a myriad of applications such as fine chemicals and materials synthesis,[1–6] separation and purification,[7–10] and chemical and biological screening.[11–14] The precise manipulation of bubbles, droplets or immiscible fluid streams in microfluidic chips is usually achieved by elaborate chip designs that well address fluid–fluid hydrodynamics under laminar flow conditions and fluid–solid interactions in engineered microchannels.[1,11] The confinement of multiple phases in microchannels creates an extremely high interface area that enhances mass transfer and reactions between phases and allows for good control over mixing inside each phase, subsequently leading to improved system performance (*e.g.*, increased reaction conversion/selectivity, favorable product structure/quality, enhanced separation efficiency, and fast diagnosis).[1–16]

The majority of the reported multiphase microfluidic systems deal with gas–liquid or liquid–liquid flow processing as specified by a number of applications such as two-phase reaction,[2–4] segmented flow based nanomaterials synthesis,[5,6] liquid–liquid extraction,[9,10] and droplet based biochemical analysis.[12] Therefore, numerous studies have been carried

[a] *Laboratory of Chemical Reactor Engineering, Department of Chemical Engineering and Chemistry, Eindhoven University of Technology, P.O. Box 513, 5600 MB Eindhoven, The Netherlands. E-mail: j.c.schouten@tue.nl; Tel: +31 40 247 3088*

[b] *School of Chemistry and Chemical Engineering, Queen's University Belfast, Belfast BT9 5AG, UK*

† Electronic supplementary information (ESI) available: Supplementary notes S1–S4, movies S1–S7. See DOI: 10.1039/c3lc51307f

out to elucidate the hydrodynamic aspects of gas–liquid and liquid–liquid flows in microchannels including, among others, flow patterns,[17–22] pressure drop,[21–27] bubble/droplet generation and transport.[28–32]

Gas–liquid–liquid three-phase flow in microfluidic systems remains as a less explored area and has received growing interest in recent years due to its important implications for various chemical and biochemical applications.[33–43] Önal *et al.*[33] reported hydrogenation of α,β-unsaturated aldehydes over a homogeneous catalyst in capillary microfluidic reactors with a diameter of 500–1000 μm. A three-phase flow was observed featuring the alternating passage of hydrogen bubbles and a catalyst containing aqueous droplets encapsulated in a continuous organic phase (aldehyde) that wetted the wall. This microfluidic system provided a rapid tool for catalyst screening and reaction kinetic studies. A similar three-phase flow pattern has been utilized for biological screening in microfluidic chips, where gas bubbles were introduced as spacers to separate reagent containing droplets dispersed in a carrier liquid.[34] This approach enables rapid testing of chemical reactions in a scalable fashion. The use of an inert gas to break up an otherwise liquid–liquid segmented or parallel flow in microchannels was shown to yield better efficiency for extraction between immiscible liquids due to an additional energy input into the system.[35–37] Over the last 5 years, microfluidic gas–liquid–liquid flow has been increasingly used for the controllable formation of composite emulsions that contain bubbles and droplets suspended in a continuous fluid phase, allowing to generate thin-shell covered microbubbles and hollow particles that can find wide uses in pharmaceuticals, as energy-storage materials and as drug delivery carriers.[38–44]

The above examples demonstrate several promising application areas for gas–liquid–liquid microfluidic systems. However, there exist a rather limited number of publications dealing with the design, operation and/or performance of three-phase flow in microchannels, with the microfluidic systems being far from fully optimized. This is largely due to the current inadequate understanding on the underlying hydrodynamics. The fundamental laws governing the three-phase generation and flow in microchannels are not yet understood due to their complex nature. The influence of flow rate on the size of bubbles or droplets produced under a three-phase flow has been revealed with some empirical correlations thereof being proposed.[41–43,46,47] However, the influence of other parameters, such as fluid properties and the geometry of an inlet mixer, was rarely taken into account.

To the best of our knowledge, no studies in the literature have suggested a model for the calculation of the three-phase pressure drop in a microchannel. Such calculation requires that phase distribution and flow regime be known at each point along the microchannel. Therefore in this paper, the hydrodynamics of the nitrogen–decane–water flow has been studied in a glass microfluidic chip which features a long microchannel with a hydraulic diameter of 98 μm connected to a cross-flow mixer. Several three-phase flow patterns will be presented, which seem not to have been reported before. The range of existence of different three-phase flow patterns is explained based on the relevant two-phase flow pattern maps observed in the absence of the third phase under otherwise identical flow conditions. Then, for each of the stable three-phase flow pattern, a pressure drop model is developed based on the corresponding two-phase (slug or parallel flow) models for the case of low capillary and Weber numbers. The developed models take into account the hydrodynamic features of the relevant three-phase flow patterns rather than being simply based on a pseudo-homogeneous approach. Finally, an example is demonstrated where the pressure drop models are employed in the design of bifurcated microchannels operated under three-phase flow conditions.

Experiment

Design of the microfluidic chip

The microfluidic chip was designed and provided by Chemtrix B.V. (The Netherlands). It comprises fluidic microchannels etched on a borosilicate glass substrate using HF. As schematically shown in Fig. 1a, the microfluidic network is composed of a long serpentine microchannel (70 cm in length) that is fed with an inlet cross-flow mixer and ends at Port F. The cross-flow mixer allows bringing three fluids introduced from ports A, B, and C into contact. The distances from the cross-flow mixer to ports A, B and C are 8, 1.6, and 8 mm, respectively. The serpentine microchannel is further connected with two other outlet ports (D and E) along its length at distances of 12.1 and 48.6 cm from the cross-flow mixer *via* short microchannel sections. In case of a reaction test, port D can be used for sampling, port E for collecting product, and port F for introducing liquid to quench the reaction. All microchannels on the chip are of the same cross-sectional dimension and are approximately rectangular in shape with a rounded bottom due to the isotropic etching process (top width: W = 300 μm; height: H = 60 μm; two side walls: 1/4 circular arc with a radius equal to H). This gives a hydraulic diameter (d_h) of 98 μm (calculations shown in ESI† note S1). The sealing of the chip was done by bonding the glass substrate having etched microchannels with a glass cover plate. Thus the formed chip was inserted into a holder (not shown in Fig. 1a) to provide interfaces with external fluidic connections.

Multiphase flow study in the microfluidic chip

The nitrogen–decane–water three-phase flow was investigated in the chip as a model three-phase system, for which the setup is also shown in Fig. 1a. Water and decane were delivered using separate syringe pumps (Fusion 200, Chemyx), where the liquid back flow was prevented by the presence of inline check valves (CV-3500, Idex Health & Science). Water and decane were introduced into the chip *via* ports A and C, respectively, through two separate poly(ether ether ketone) (PEEK) capillaries 1 and 3 (inner diameter: 150 μm; length: 30 cm). Nitrogen was delivered from a gas cylinder and its

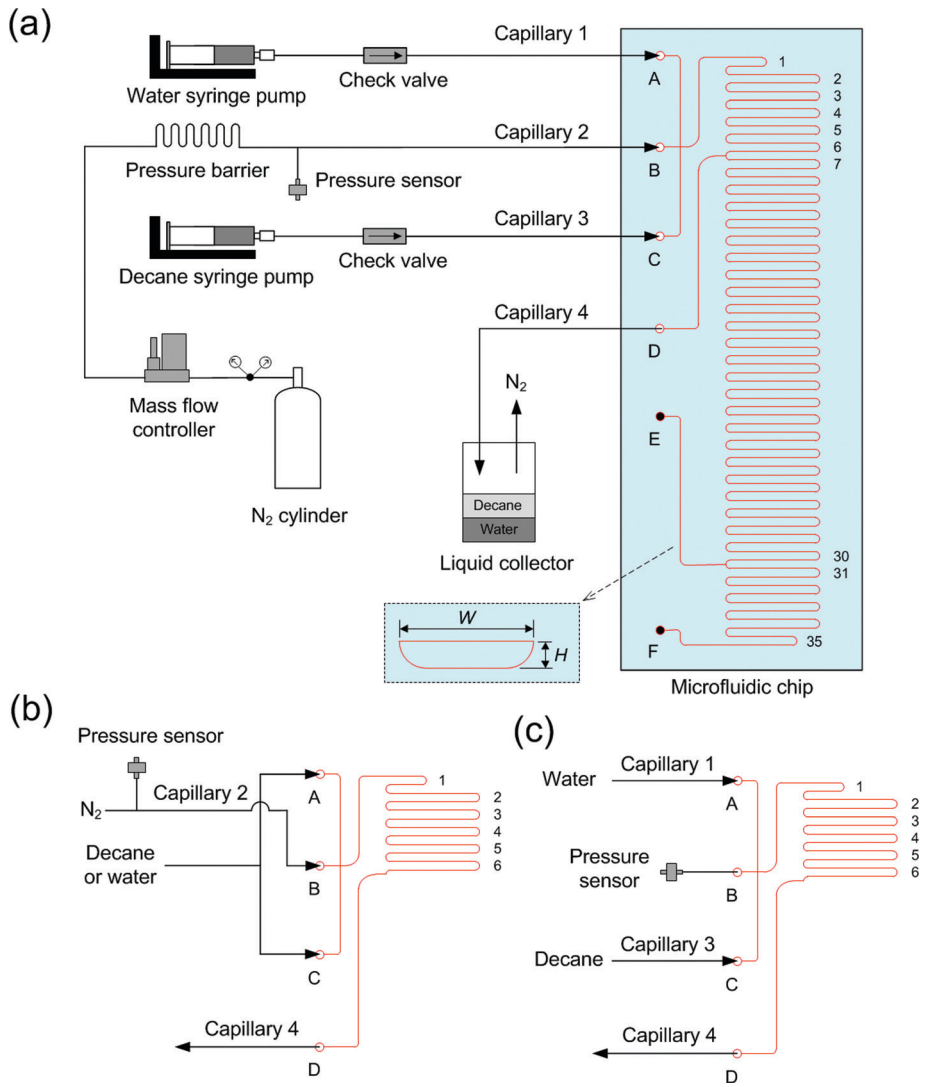

Fig. 1 Schematic view of the experimental setup for the two-phase and three-phase flow studies in the microfluidic chip. (a) Nitrogen–decane–water flow. Ports E and F on the chip are blocked and therefore not in use. The microchannel cross section is shown in the dashed box. (b) Nitrogen–water or nitrogen–decane flow. (c) Decane–water flow. In (b) and (c), only the fluidic connections with a pressure sensor and the used part of the microchannel that bears two-phase flow are shown. The unused part of the chip is not shown for brevity.

flow rate was regulated by a mass flow controller (EL-Flow, Bronkhorst). To ensure a constant gas flow rate unaffected by possible multiphase flow fluctuations in the chip, a large pressure barrier was added in the gas feeding line using a small-diameter PEEK capillary (inner diameter: 25 μm; length: 30 cm). The pressure drop in this capillary was approximately one order of magnitude larger than that of the three-phase flow in the chip under the investigated conditions. The gauge pressure in the gas feeding line right after the pressure barrier was measured with a pressure sensor (26PC, Sensortechnics). Nitrogen was introduced into the chip *via* port B through PEEK capillary 2 (inner diameter: 150 μm; length: 37 cm). After being generated at the cross-flow mixer, the three-phase mixture travelled along the serpentine microchannel and was guided out of the chip *via* port D whereas ports E and F were not in use (blocked). The three-phase mixture out of the chip was discharged into an open flask through PEEK capillary 4 (inner diameter: 150 μm; length: 15 cm). Therefore in the current flow arrangement, the three-phase flow was only present in segments 1–6 of the serpentine microchannel and the subsequent short connecting microchannel (1.9 mm long) leading to port D, which yields an effective microchannel with a total length (L) of 14 cm for the three-phase flow to travel through. The remaining part of the chip (segments 7–35 of the serpentine microchannel plus the connecting microchannel leading to port E) was filled with water during the experiments and thus no flow was present there. Note that each segment represents a set of two straight microchannel sections, the two ends of which are both fed with curved microchannel sections (1/4 circular arc), except segments 1 and 35 which end at the cross-flow mixer and port F, respectively. This flow arrangement allowed us to measure the pressure drop in the three-phase flow below 0.1 MPa under the investigated conditions. Otherwise, the measured pressure drop would be much

higher if the entire serpentine microchannel is used, which will induce a significant variation of the gaseous volumetric flow rate along the microchannel and might cause an axial change in the three-phase flow pattern leading to additional difficulties in the pressure drop analysis (this could be a next step following the present study and will not be dealt with here).

The experiments were performed under ambient conditions (~20 °C, 0.1 MPa). The volumetric flow rates of water and decane (*i.e.*, Q_W and Q_D) are both in the range of 0.6 to 40 μl min^{-1}, with the gas flow rate being fixed at three given values (30, 60, and 90 μl min^{-1} at standard conditions). This corresponds to a superficial velocity of decane (j_D) and that of water (j_W) both in the range of 0.6 to 40.5 mm s^{-1}, and a superficial gas velocity at standard conditions ($j_{G,STP}$) varying from 30.4 to 91.2 mm s^{-1}, which are obtained by dividing the volumetric flow rate by the cross-sectional area of the microchannel.

Three-phase flow images were visualized by an inverted microscope (Axio Observer D1m, Carl Zeiss) coupled with a high speed imaging camera (MotionPro CCD, Redlake). The chip with its holder was fitted to a translation stage of the microscope, allowing the image acquisition at different sections within the chip under the light transmission mode.

To further explain the observed three-phase flow pattern and its pressure drop behavior, two-phase flow (of the nitrogen–water, nitrogen–decane, and decane–water systems) was studied in the chip under similar operational conditions to the three-phase flow study. Fig. 1b and c depict the fluidic connection with the chip and pressure measuring method for each two-phase flow study. In the case of the nitrogen–decane or nitrogen–water flow, the liquid was divided into two substreams being introduced into the chip *via* ports A and C. Nitrogen was introduced into the chip *via* port B using capillary 2 and the pressure was measured in the feeding line (Fig. 1b). In the case of liquid–liquid flow, water and decane were introduced into the chip *via* ports A and C using capillaries 1 and 3, respectively. The central port B was connected with the pressure sensor to indicate the pressure in the cross-flow mixer (Fig. 1c). The two-phase mixture flowed out of the chip *via* port D and was guided into the outlet capillary 4 before being discharged. Thus the flow route in the chip here is the same as that in the three-phase flow study. The unused part of the chip (segments 7–35 of the serpentine microchannel plus the connecting microchannel leading to port E) was filled with water during the nitrogen–water or decane–water flow, and was filled with decane during the nitrogen–decane flow. Other flow schematics, apparatus in use, and the flow rate ranges remained unchanged compared to those in the three-phase flow study.

Reference experiments for the deduction of pressure drop in the microfluidic chip

In the three-phase flow study described above, the reading of the pressure sensor (*cf.* Fig. 1a) designates the total pressure drop which consists of contributions from: (i) nitrogen flow in the inlet capillary 2; (ii) nitrogen flow from port B to the cross-flow mixer of the chip; (iii) three-phase flow in the chip; (iv) three-phase flow in the outlet capillary 4; and (v) local entrance/exit losses. While the contributions from (i), (ii) and (v) can be neglected under the investigated conditions, the contribution from (iv) has to be measured in order to deduce the pressure drop associated with three-phase flow in the chip. This has been done by performing the reference three-phase flow experiments without the chip using the setup shown in Fig. 1a and an external PEEK cross-flow mixer (1.25 mm in diameter; each fluid branch about 4 mm long) replaced the chip in order to keep the current fluid arrangement (*i.e.*, four ports of the mixer were connected with capillaries 1–4). The total frictional pressure drop of the three-phase flow in the current microchannel (L = 14 cm) was then obtained as the difference in pressure measurements with and without the chip under identical flow rate conditions, which is based on an ideal assumption that the hydrodynamics of three-phase flow remained the same in the outlet capillary 4 during experiments with and without the chip.

The pressure drop of the two-phase flow in the current microchannel was obtained in a similar manner by performing pressure measurements with and without the chip at the same flow rate conditions using the setup shown in Fig. 1b and c. A justification of this pressure drop deduction method has been shown before for gas–liquid and liquid–liquid flow studies in microchannels.[18,27]

Results and discussion

Three-phase flow pattern: analogy with gas–liquid and liquid–liquid flows

Representative images of three-phase flow observed in the microfluidic chip are shown in Fig. 2. Two major flow patterns are identified as the three-phase slug flow and parallel-slug flow under the investigated conditions.

The three-phase slug flow appeared especially when j_W was significantly higher than j_D for a given $j_{G,STP}$ (*e.g.*, at j_D = 10.1 mm s^{-1}, j_W = 40.5 mm s^{-1}, and $j_{G,STP}$ = 30.4 mm s^{-1}, see Fig. 2a). This flow pattern was normally generated at the downstream location after the cross-flow mixer (*i.e.*, at a distance of about 2–12 mm from the cross-flow mixer well before the flow reached the right part of segment 1) by the breakup of the previously formed parallel flow of water with respect to the decane carrying travelling nitrogen bubbles (as also shown in ESI† movies S1–S2). A three-phase slug flow was then seen through segments 1–6 and the short connecting microchannel leading to the outlet port D of the chip, which is characterized by the alternate movement of water slugs and decane droplets encapsulating nitrogen bubbles (as also shown in ESI† movies S3–S4). Water is the continuous phase due to its good wettability on glass, which is also justified by the convex ends of decane droplets. A thin decane film is present between the bubble body and the surrounding water film that wetted the wall. One elongated bubble was included in one

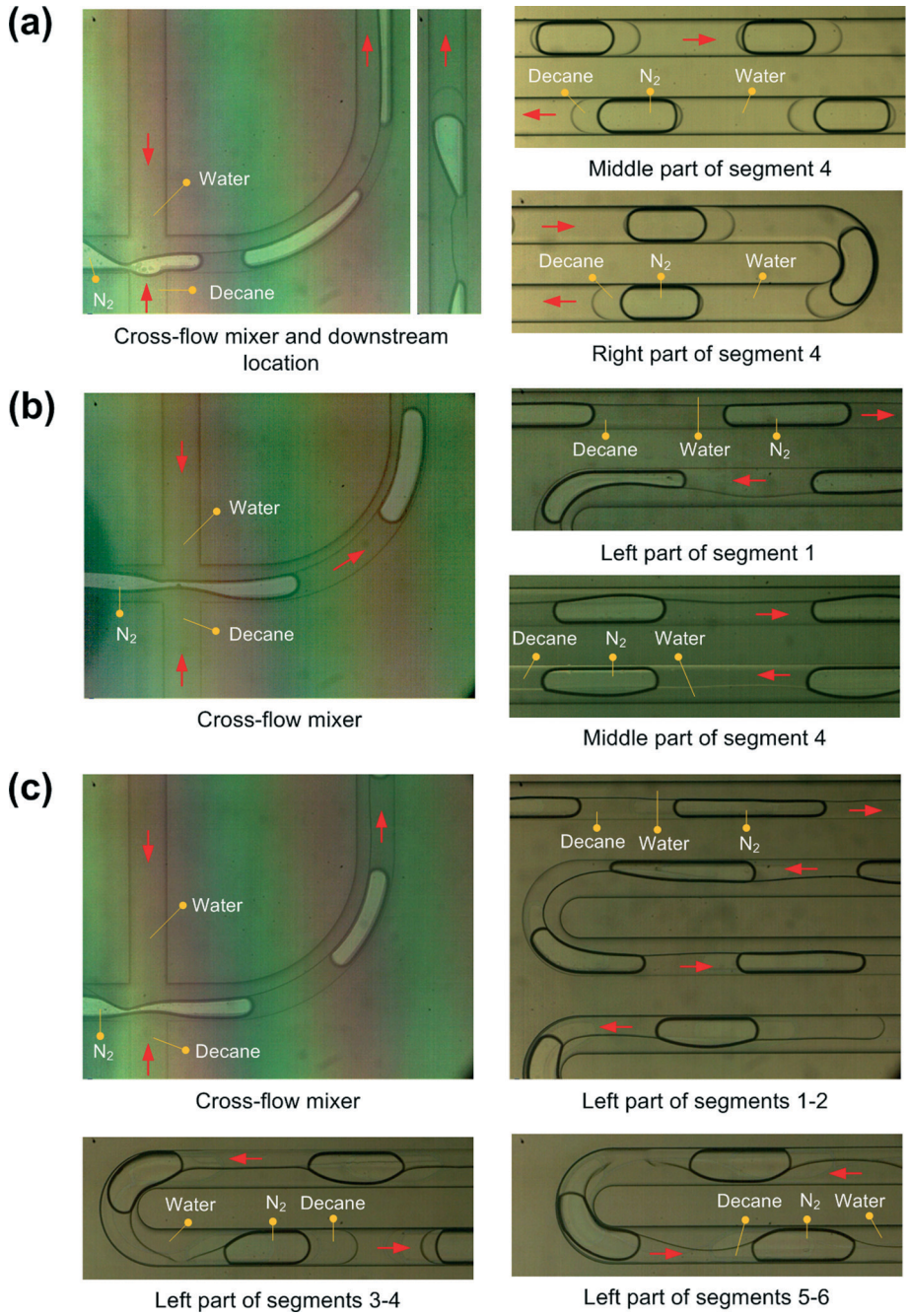

Fig. 2 Microscope images of the three-phase flow patterns in the chip. (a) Three-phase slug flow. $j_{G,STP}$ = 30.4 mm s^{-1}, j_D = 10.1 mm s^{-1}, j_W = 40.5 mm s^{-1}. Downstream location refers to the microchannel section at a distance of 5 mm from the cross-flow mixer. (b) Parallel-slug flow. $j_{G,STP}$ = 30.4 mm s^{-1}, j_D = 30.4 mm s^{-1}, j_W = 15.2 mm s^{-1}. (c) Transitional flow between three-phase slug flow and parallel-slug flow. $j_{G,STP}$ = 30.4 mm s^{-1}, j_D = 20.3 mm s^{-1}, j_W = 20.3 mm s^{-1}. The red arrows indicate the flow direction. In (c), the left part of segments 3–4 and 5–6 is shown with only one microchannel section for each segment.

decane droplet in most cases and thus the formed composite is termed as the 'nitrogen-in-decane' droplet. This flow pattern seems not to have been reported in microfluidic chips before, although its equivalent was observed in large diameter capillaries (≥1 mm).[48] In the existing study of the microfluidic three-phase flow, a train of discrete bubbles and droplets or spherical bubbles encapsulated in spherical droplets is usually found in a flow.[33–47]

The parallel-slug flow appeared especially when j_W was significantly lower than j_D for a given $j_{G,STP}$ (*e.g.*, at j_D = 30.4 mm s^{-1}, j_W = 15.2 mm s^{-1}, and $j_{G,STP}$ = 30.4 mm s^{-1}, see Fig. 2b). This flow pattern features a side-by-side flow between decane and water with elongated nitrogen bubbles travelling in the decane phase. This flow pattern, once generated at the cross-flow mixer (*i.e.*, by forming a parallel flow of water with respect to decane and by the breakup of the gas neck to produce

bubbles in decane), was sustained throughout the chip (as also shown in ESI† movies S5–S7). The decane–water interface was generally in parallel to the flow direction (as viewed from the top surface of the microchannel) except near the curved sections of the microchannel at which the width of the water stream was likely to change to some extent (see segment 1 in Fig. 2b). The interface remained almost immobilized except sometimes when the bubble passed by. In other words, bubbles at the downstream segments sometimes were seen to further expand towards the water side causing a temporarily curved decane–water interface (see segment 4 in Fig. 2b). Such change of shape of the bubbles could be due to an increase in the actual superficial gas velocity along the microchannel given the significant pressure drop therein (being 35 kPa under the conditions relevant to Fig. 2b). A similar flow pattern was also observed by Wang *et al.*[47] during the flow of an air–aqueous polyethylene glycol solution-mixed oil system in a very short microchannel fed with a cross-flow mixer, but the bubbles in their work appeared to be much shorter in size.

A transitional flow pattern between the three-phase slug flow and parallel-slug flow was found when j_W and j_D were comparable for a given $j_{G,STP}$ (*e.g.*, at $j_D = j_W = 20.3$ mm s^{-1} and $j_{G,STP} = 30.4$ mm s^{-1}, see Fig. 2c). Parallel-slug flow generated at the cross-flow mixer was seen to travel along the beginning segments (see segments 1–2 in Fig. 2c), which further destabilized downstream and changed into three-phase slug flow after the breakup of the decane thread. A spatial–temporal change in the breakup behavior was observed. The breakup could occur in different segments at different moments and could produce decane droplets containing only one or multiple bubbles (see segments 3–4 and 5–6 in Fig. 2c).

Fig. 3a–c present the gas–liquid–liquid flow pattern map as a function of j_W and j_D for three different values of $j_{G,STP}$ at 30.4, 60.8, and 91.2 mm s^{-1}, respectively. The three-phase slug flow pattern was observed at j_D (ranging from about 0.6 to 10.1 mm s^{-1}) typically lower than j_W for each given $j_{G,STP}$. The parallel-slug flow pattern was observed at j_D (ranging from about 2.5 to 40.5 mm s^{-1}) typically higher than j_W for each $j_{G,STP}$. The flow pattern shifted from the three-phase slug flow to parallel-slug flow with the transitional flow pattern in between upon increasing j_D at a constant j_W or upon decreasing j_W at a constant j_D. This could be understood as follows: at relatively low j_D (*e.g.*, at $j_D < j_W$), the breakup of the emerging decane droplet tended to take place at a short distance after the cross-flow mixer (*cf.* Fig. 2a), leading to the formation of a three-phase slug flow; at intermediate values of j_D (*e.g.*, at $j_D \approx j_W$), the advancing decane tip travelled farther due to increased momentum and the breakup occurred in different segments (*cf.* Fig. 2c), leading to the formation of a transitional flow pattern; at relatively high j_D (*e.g.*, at $j_D > j_W$), the breakup could not occur throughout the chip as the advancing decane tip far reached the outlet port D, thus creating a parallel-slug flow (*cf.* Fig. 2b). It also appeared from Fig. 3a–c that the existence region of the transitional flow pattern seems to be enlarged at increased $j_{G,STP}$ especially when j_W and j_D are both comparatively low whereas the regions for the other two major flow patterns tend to shrink (*e.g.*, at both j_W and j_D lower than 5 mm s^{-1}, and $j_{G,STP}$ = 91.2 mm s^{-1}, see Fig. 3c). This implies that a comparatively

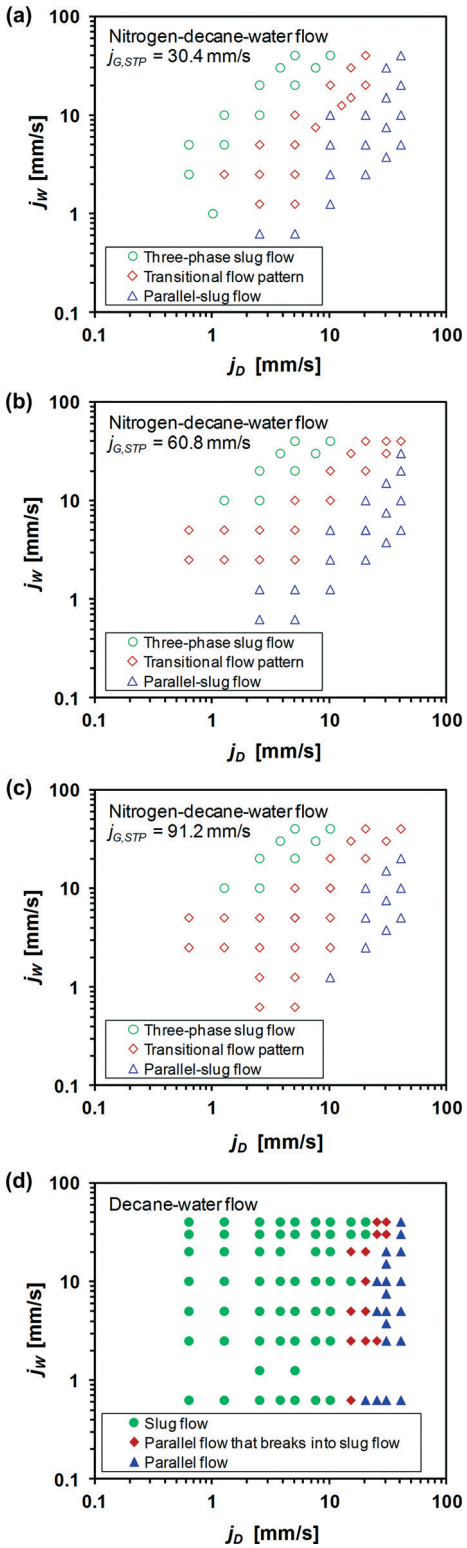

Fig. 3 (a)–(c) Nitrogen–decane–water flow pattern maps as a function of j_W and j_D observed in the chip for three different values of $j_{G,STP}$. (d) Decane–water flow pattern map.

small gas flow rate (*e.g.*, $j_{G,STP} \leq 30.4$ mm s^{-1}) is favorable for the formation of a stable three-phase slug flow or a parallel-slug flow.

To explain the presence of the identified three-phase flow patterns, an experimental study of a two-phase flow through this chip has been conducted. It became clear that under the current operational conditions, the relevant decane–water flow pattern turned out to be a slug flow, a parallel flow that breaks into a slug flow inside the microchannel, and a parallel flow, as shown in the flow pattern map (Fig. 3d). At a given j_W, a decane–water slug flow was generated at the cross-flow mixer and travelled in the chip at relatively low j_D (Fig. 4a). As j_D was increased, a decane–water parallel flow was first seen in the beginning segments after its formation at the cross-flow mixer, which could further break into a slug flow in the following segments (Fig. 4b). If j_D was sufficiently high, this breakup did not take place and a parallel flow was sustained throughout the chip (Fig. 4c). These observations

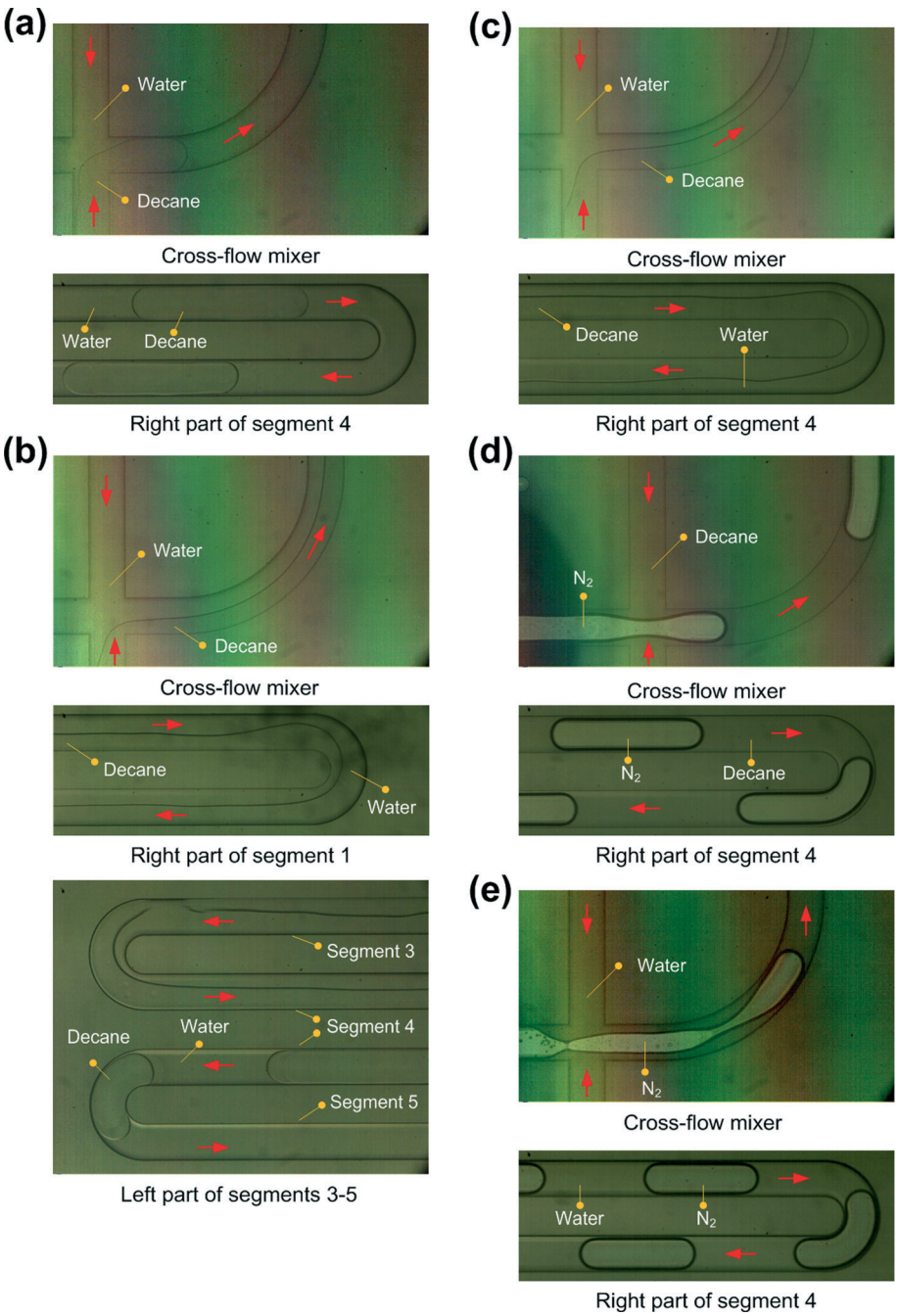

Fig. 4 Microscope images of the two-phase flow patterns in the chip. (a) Decane–water slug flow. j_D = 10.1 mm s^{-1}, j_W = 20.3 mm s^{-1}. (b) Decane–water parallel flow that breaks into slug flow in the microchannel. j_D = 20.3 mm s^{-1}, j_W = 20.3 mm s^{-1}. (c) Decane–water parallel flow. j_D = 30.4 mm s^{-1}, j_W = 15.2 mm s^{-1}. (d) Nitrogen–decane slug flow. $j_{G,STP}$ = 30.4 mm s^{-1}, j_D = 40.5 mm s^{-1}. (e) Nitrogen–water slug flow. $j_{G,STP}$ = 30.4 mm s^{-1}, j_W = 40.5 mm s^{-1}. The red arrows indicate the flow direction.

are consistent with the findings of Guillot and Colin,[49] who described a similar breakup of a parallel flow into a slug flow in a microchannel by a blocking–pinching mechanism. Moreover, the relevant flow patterns for the nitrogen–decane flow and the nitrogen–water flow in the chip were found to be always a slug flow under the investigated flow rate conditions for a three-phase flow (*cf.* Fig. 4d and e). As the surface tension for the nitrogen–decane system (~24 mN m^{-1}) is much lower than that for the nitrogen–water system (~73 mN m^{-1}), nitrogen bubbles were preferably generated in the decane phase in the case of the three-phase flow. This would require overcoming smaller capillary pressure for the bubble formation.

Then, the distribution of each flow pattern on the three-phase flow pattern map can be well explained: the three-phase slug flow is a superimposition of both decane–water and nitrogen–decane slug flows that prevailed under the relevant two-phase flow conditions; the parallel-slug flow is a superimposition of the decane–water parallel flow and the nitrogen–decane slug flow; and the transitional flow pattern found between the three-phase slug flow and parallel-slug flow is a combination of the nitrogen–decane slug flow and the transitional water–decane flow (*i.e.*, a parallel flow that breaks into a slug flow in the microchannel). One can further see from Fig. 3a–d that the addition of nitrogen gas has caused the transition between each three-phase flow pattern to shift towards lower j_D at a given j_W as compared with the case of the decane–water flow. This can be understood by the presence of nitrogen bubbles in either a dispersed decane droplet (in the case of a three-phase slug flow) or a continuous decane stream (in the case of a parallel-slug flow), which increases the effective flow rate on the decane side as compared to that on the water side leading to such an early flow pattern transition.

Some promising applications of the identified major three-phase flow patterns would be in multiphase catalysis, synthesis, and separation, where typical examples are envisaged as intensification of liquid–liquid extraction by gas agitation,[35–37] reaction kinetic studies in organic synthesis *via* aqueous catalysis in a three-phase mode (*e.g.*, hydrogenation,[33] hydroformylation,[50] and oxidation[51]) and nanomaterial synthesis in liquid–liquid systems involving a gaseous reducing agent (*e.g.*, CO).[52] It is worth mentioning that for specific applications, it might be preferable to generate a three-phase slug flow with bubbles in the aqueous droplets or to generate a parallel-slug flow with bubbles in the aqueous stream. This can be realized by tuning the surface wetting properties of microchannels on the chip and/or by modifying the interface tension properties of the fluid pairs.

Pressure drop under a three-phase slug flow: analogy with a two-phase slug flow

Currently, no specific pressure drop model has been developed for gas–liquid–liquid flow in microchannels. The derivation of a pressure drop model for a three-phase slug flow is done in two steps: first, a two-phase pressure drop model describing the experimental measurements during gas–liquid and liquid–liquid slug flows in the current chip is developed; second, this model is extended towards a three-phase slug flow by further considering the 'nitrogen-in-decane' droplet in this flow pattern as a pseudo-homogeneous droplet with an effective viscosity.

Pressure drop model for a two-phase slug flow

It is known that for a two-phase slug flow through a microchannel, the total frictional pressure drop (ΔP_{tot}) is the summation of the pressure drop in the liquid slug (ΔP_S), the pressure drop across the bubble or droplet body (ΔP_{body}), and the excess pressure drop over the end caps of bubbles or droplets (ΔP_{caps}).[23–27] That is,

$$\Delta P_{tot} = \Delta P_S + \Delta P_{body} + \Delta P_{caps} \quad (1)$$

The pressure drop in the liquid slug is calculated using the Hagen–Poiseuille type equation under fully-developed laminar flow condition:

$$\Delta P_S = \frac{nC\mu_C L_S U_S}{2d_h^2} \quad (2)$$

where μ_C is the viscosity of the continuous phase (*i.e.*, the liquid slug) and L_S is the slug length. U_S is the average velocity in the liquid slug ($U_S = j_W + j_D$ for the decane–water slug flow in the current microchannel; $U_S = j_G + j_D$ or $U_S = j_G + j_W$ for the nitrogen–decane or nitrogen–water slug flow, respectively, where j_G is the average superficial velocity of the nitrogen evaluated using the density under the average pressure in the microchannel). C is the laminar friction constant which was determined to be about 75.33 *via* Comsol simulation for the present microchannel cross section (see ESI† note S1 for our Comsol simulation on the laminar flow of water in the chip). n is the number of slug flow unit cells (*i.e.*, one bubble plus one liquid slug, or one droplet plus one liquid slug) present in the microchannel and is calculated from

$$n = \frac{L}{L_D + L_S} \quad (3)$$

Here L is the total length of the active microchannel on the chip bearing a two-phase or three-phase flow (= 14 cm; *cf.* Fig. 1a). L_D represents the length of the dispersed phase (= L_B for gas–liquid slug flow; = L_{drop} for liquid–liquid slug flow; where L_B and L_{drop} are the bubble or droplet length, respectively; *cf.* insets in Fig. 5a and b).

The calculation of the laminar pressure drop across the body of a bubble or a droplet within a slug flow can be simplified by neglecting the presence of the surrounding liquid film as a first approximation.[25,31] This leads to

$$\Delta P_{body} = \frac{nC\mu_D L_{body} U_D}{2d_h^2} \quad (4)$$

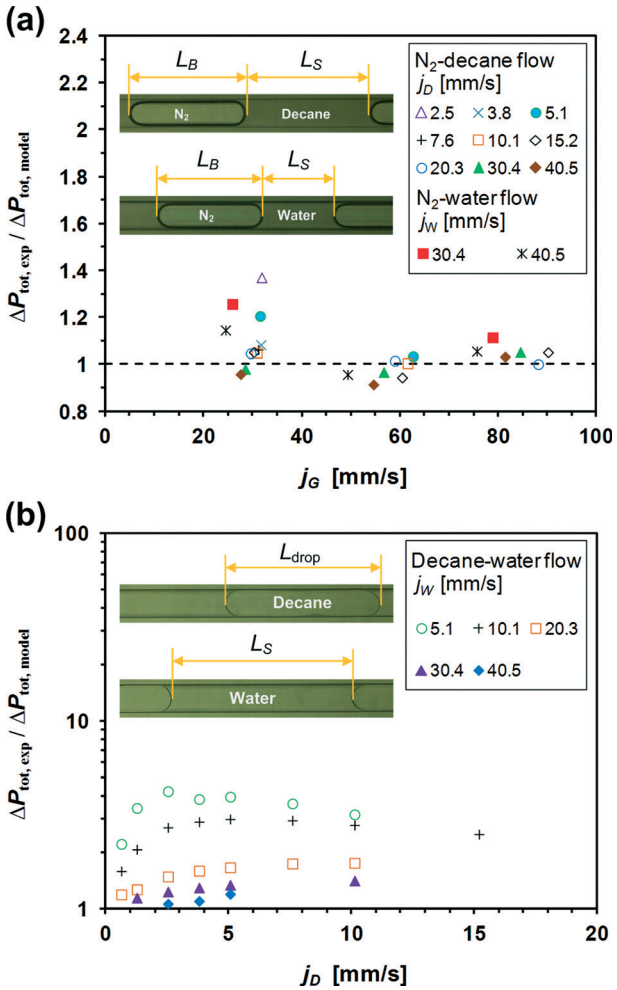

Fig. 5 The total frictional pressure drop under the two-phase slug flow in the chip. Symbols represent the ratio between the experimental measurements and the model predictions by eqn (6) as a function of the corresponding superficial velocity. The dashed line represents the parity line. (a) Nitrogen–decane and nitrogen–water slug flows. (b) Decane–water slug flow. The insets show the flow images from which L_S and L_D (= L_B for gas–liquid slug flow; = L_{drop} for liquid–liquid slug flow) were obtained. The experimental data represent the area where a stable slug flow pattern was observed throughout the current microchannel (*i.e.*, no bubble/droplet coalescence or breakup, consistent bubble or droplet size).

where μ_D is the viscosity of the dispersed phase and U_D the bubble or the droplet velocity (= U_B for gas–liquid slug flow; = U_{drop} for liquid–liquid slug flow; where U_B and U_{drop} are the bubble or droplet velocity, respectively). L_{body} refers to the length of the body of a bubble or a droplet and can be approximated as $L_{body} \approx L_D - d_h$ (*cf.* insets in Fig. 5a and b).

In the limit of negligible capillary numbers (Ca = $\mu_C U_D/\sigma$; where σ is the interface tension) and negligible inertia effects, the pressure drop over the end caps of a bubble moving through a rectangular microchannel ($H \leq W$; where H and W are the channel height and width, respectively) can be described by[53]

$$\Delta P_{caps} = c_1 \frac{n \mathrm{Ca}^{2/3} \sigma}{H} \quad (5)$$

where c_1 is a geometrical parameter. Fuerstman *et al.*[23] determined c_1 *via* experiments to be around 16 which was independent of the channel aspect ratio, H/W (see Fig. 4C in their paper; where a different symbol being c was used therein). In contrast, Wong *et al.*[53] reported a lower value of c_1 (ranging from around 6 to 7) analytically for several rectangular microchannels with aspect ratios larger than 0.5 by assuming that the resistance to bubble motion originated from liquid films and not from liquid-filled corners. It is expected that eqn (5) can be applied for the estimation of the interfacial pressure drop in the current microchannel as its cross section is close to being rectangular (*cf.* Fig. 1a), which is also based on the consideration that the laminar friction constant determined for the current microchannel is very close to that for a rectangular microchannel with the same aspect ratio (as shown in ESI† note S1). The same eqn (5) is valid in estimating the pressure drop over the end caps of a low viscosity droplet (*e.g.*, at $\mu_D/\mu_C < 1$).[54] Hereafter, we will use eqn (5) with $c_1 = 16$ according to the finding of Fuerstman *et al.*[23] for the pressure drop model development in this work as a rectangular microchannel with $H/W = 0.2$ was investigated in their work, which is very similar to the present microchannel geometry.

Then, the total frictional pressure drop associated with a two-phase slug flow in the chip is rewritten as

$$\Delta P_{tot} = \frac{L}{L_D + L_S}\left[\frac{C\mu_C L_S U_S + C\mu_D (L_D - d_h) U_D}{2 d_h^{\,2}} + c_1 \mathrm{Ca}^{2/3} \sigma / H\right] \quad (6)$$

where the constants $C = 75.33$, $c_1 = 16$ for the current microchannel, and Ca = $\mu_C U_D/\sigma$, as shown above. Fig. 5a and b present a comparison between the measured total frictional pressure drop associated with the two-phase slug flow (of the nitrogen–decane, nitrogen–water, and decane–water systems) in the chip (designated as $\Delta P_{tot,exp}$) and the model prediction by eqn (6) (designated as $\Delta P_{tot,model}$). The slug flow parameters (*i.e.*, U_D, L_D, L_S) needed in eqn (6) were measured and averaged from multiple images captured in the middle part of microchannel segments 3–5 (*cf.* Fig. 1a). The variation of L_D and L_S with the operating conditions is shown in ESI† note S2.

In the case of the nitrogen–decane and nitrogen–water slug flows (Fig. 5a), the experimental measurements are well represented by eqn (6) given the $\Delta P_{tot,exp}/\Delta P_{tot,model}$ ratio ranging from about 0.9 to 1.2 under most conditions. It is worth mentioning that eqn (6) is applicable under low capillary numbers and negligible inertial effects (*i.e.*, at Ca $\ll$ 0.1 and We $\ll$ 1, where We = $d_h U_D^{\,2} \rho_C/\sigma$ is the Weber number; where ρ_C is the density of the continuous phase). As shown in Table 1, this limiting condition is roughly satisfied in both gas–liquid and liquid–liquid slug flow experiments under the operating conditions relevant to Fig. 5a and b. One may argue that eqn (6) tends to yield a somewhat underestimation in ΔP_{tot} arising from the simplification in the calculation of ΔP_{body} with eqn (4). In the current slug flow experiments, the

bubble was indeed surrounded by a liquid film (although not thick due to low Ca numbers involved), as evidenced in Fig. 6a that the bubble moved faster than the liquid slug (*i.e.*, $U_D > U_S$).[24] Therefore, the bubble body could not fill the entire microchannel cross section, which is likely to yield a somewhat higher pressure drop than the prediction of eqn (4) (a more accurate calculation in ΔP_{body} can be achieved based on the laminar–laminar annular flow solution to the velocity profile in the bubble body as already shown for circular microchannels[55]). However, due to the much lower viscosity of nitrogen than that of the liquid, ΔP_{body} is negligible compared with the other two contributions from ΔP_S and ΔP_{caps}. The calculated ΔP_{body} with eqn (4) is well below 10% of $\Delta P_{tot,exp}$ under the majority of conditions in the gas–liquid slug flow experiments and thus such underestimation does not appreciably deteriorate the model performance. It is worth mentioning that the relative contribution of the three pressure drop terms (*i.e.*, ΔP_S, ΔP_{body} and ΔP_{caps}) depends on the slug flow characteristics for a given gas–liquid or liquid–liquid system. The overall pressure drop could be dominated by ΔP_{body} if the droplet length is sufficiently larger than that of the liquid slug. However this situation is seldom realized in practice during the gas–liquid flow due to the low viscosity of bubbles. As ΔP_{caps} scales with $Ca^{2/3}$ whereas ΔP_S and ΔP_{body} scale approximately with Ca (see eqn (2), (4) and (5) where U_S is assumed approximately equal to U_D), there might exist a critical value of Ca above which ΔP_{caps} can be neglected when compared with the other two terms. Note that for a given system, the Ca number merely depends on U_D, with other parameters being fixed.

In the case of the decane–water slug flow (Fig. 5b), the experimental measurements are best described by the model predictions only at the highest j_W of 40.5 mm s^{-1} under investigation. $\Delta P_{tot,exp}$ tends to be significantly higher than $\Delta P_{tot,model}$ upon further decreasing j_W or increasing j_D. This deviation could be explained by the underestimation of ΔP_{body} with eqn (4) which does not consider the additional pressure drop induced by the dewetting and rupture of the water film surrounding the decane droplet in this case. As shown in Table 1, the decane–water slug flow was realized in the chip under relatively low capillary numbers ($Ca < 1 \times 10^{-3}$) compared with the case of gas–liquid flow. Thus the liquid film is expected to be very thin (as also corroborated by the fact that U_D is close to U_S, see Fig. 6a) and tends to be metastable, under which the dewetting process is likely to occur.[56] A direct proof of the dewetting can be seen from representative images shown in Fig. 6b–j. When the decane droplet travelled down the microchannel, the water film that was shed from the preceding water slug first lubricated the decane

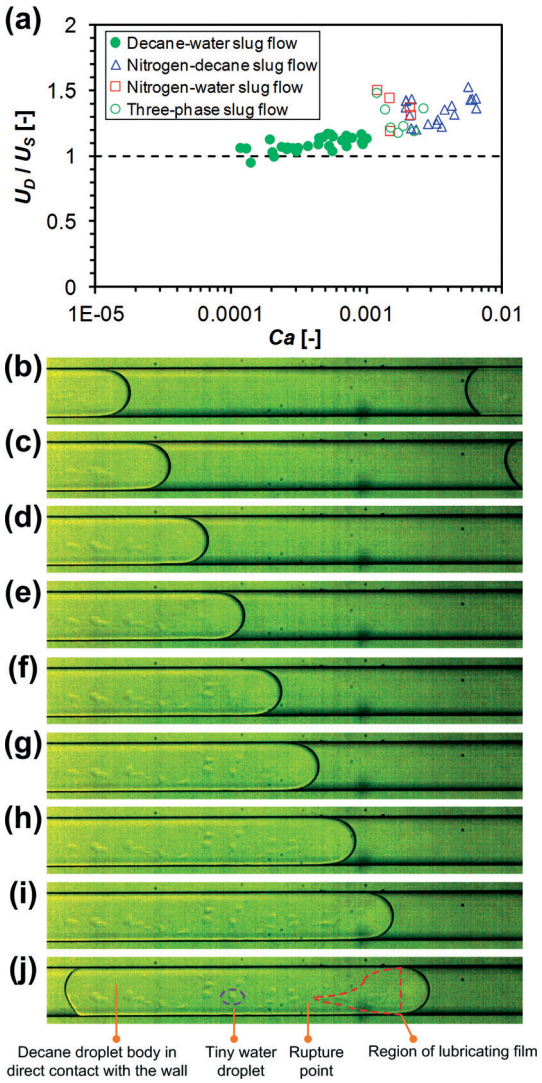

Fig. 6 (a) The measured U_D/U_S ratio as a function of the capillary number (Ca) for the two-phase and three-phase slug flows in the chip. U_D is the bubble or droplet velocity (= U_B for gas–liquid slug flow; = U_{drop} for liquid–liquid or three-phase slug flow). For three-phase flow, U_{drop} means the velocity of the 'nitrogen-in-decane' droplet. Symbols represent the results of this work and the dashed line represents a U_D/U_S ratio of 1. (b)–(j) Dewetting process of the water film around the decane droplet body. The images of the decane–water slug flow were taken at 20 ms intervals in the middle part of microchannel segment 4 at $j_D = j_W$ = 5.1 mm s^{-1}. The flow direction is from left to right.

Table 1 Range of Ca, We, and Re numbers in pressure drop measurements under the two-phase and three-phase flow studies in the chip

Flow	Ca	We	Re[a]
Nitrogen–decane slug flow	1×10^{-3}–7×10^{-3}	7×10^{-3}–9×10^{-2}	3–14
Nitrogen–water slug flow	1×10^{-3}–3×10^{-3}	9×10^{-3}–4×10^{-2}	8–15
Decane–water slug flow	1×10^{-4}–1×10^{-3}	6×10^{-5}–5×10^{-3}	0.5–5
Three-phase slug flow	1×10^{-3}–3×10^{-3}	7×10^{-3}–4×10^{-2}	6–14
Parallel-slug flow	2×10^{-3}–7×10^{-3}	1×10^{-2}–1×10^{-1}	4–15

[a] Re = We/Ca is the Reynolds number.

droplet body at the front (Fig. 6b). At some point along the droplet body, the water film became unstable and dewetted, giving way to the decane droplet the body of which was in direct contact with the wall (Fig. 6c). The back of the dewetted liquid film ruptured to generate small irregular-shaped water droplets entrained between the decane droplet body and the wall. As the decane droplet moved on, it kept picking up from the front the lubricating water film which further ruptured to small water droplets (Fig. 6d–di). This finally gave rise to a number of water droplets present along the whole body of the decane droplet which otherwise would completely touch the center of the microchannel wall, thereby creating complicated liquid/liquid/solid contact lines (Fig. 6j).

Dewetting has been previously observed by Cubaud and Ho[21] for the air–water slug flow in a square microchannel ($H = W$) made of glass and silicon. They found that for this partially wetting system ($\theta > 0$, where θ is the contact angle of the continuous liquid on the wall), a liquid film below a critical thickness could dewet creating complex gas/liquid/solid three-phase contact lines if $U_{dew} < U_B < V_C$. Here, U_{dew} is the dewetting velocity that was measured to be around 7 mm s^{-1} for water dewetting on glass in an air atmosphere. V_C is the critical bubble velocity for the center of the microchannel to be dried out at the rear of the bubble, beyond which the bubble body is lubricated by a liquid film without the presence of the three-phase contact lines ($V_C \approx U_{dew}L_B/W$). The presence of the dewetting behavior in the current decane–water slug flow case could be explained by applying this criterion as well, that is, $U_{dew} < U_{drop} < V_C$ ($\approx U_{dew}L_{drop}/W$). Under the operating conditions relevant to Fig. 5b, U_{drop} is in the range of 6.1 to 51.8 mm s^{-1} and V_C is calculated to be in the range of 20 to 68.3 mm s^{-1}. It is found that this criterion is approximately satisfied for j_W = 5.1–20.3 mm s^{-1} if the same dewetting velocity of about 7 mm s^{-1} was assumed. This suggests that the dewetting and rupture of the lubricating water film would occur at such relatively low j_W, which is in agreement with our observation (as illustrated in Fig. 6b–j). Since the presence of the moving three-phase contact lines within a slug flow yields much more energy dissipation as compared to the case without contact lines,[57] it is obvious that eqn (4) tends to significantly underestimate ΔP_{body} if the dewetting occurs in the lubricating liquid film. This explains why the $\Delta P_{tot,exp}/\Delta P_{tot,model}$ ratio is significantly larger than 1 at j_W = 5.1–20.3 mm s^{-1} (Fig. 5b). Furthermore, under such range of j_W, the $\Delta P_{tot,exp}/\Delta P_{tot,model}$ ratio is seen to increase with decreasing j_W or increasing j_D. This is mainly a result of the increased decane droplet length which tends to create more three-phase contact lines along the droplet body, thereby further increasing the relative contribution of the pressure drop across the droplet body in the total frictional pressure drop. At $j_W > 20.3$ mm s^{-1}, the $\Delta P_{tot,exp}/\Delta P_{tot,model}$ ratio is close to 1 (Fig. 5b), indicating that the dewetting behavior (if present) poses less influence as the droplet velocity is increased significantly under this condition and a lubricating liquid film is likely to be present almost around the entire droplet body especially at the highest j_W of 40.5 mm s^{-1} under investigation. It has to be mentioned that the above discussion about the dewetting behavior in the case of the decane–water slug flow is rather qualitative as the dewetting velocity of a liquid film at the interface between a solid wall and another immiscible liquid might differ from that obtained at the gas–solid interface.[58–60] Although the dewetting behavior in the latter situation is well understood, the dewetting of a liquid film at solid–liquid interfaces has received little attention[60] and a detailed study of this phenomenon is beyond the scope of this work.

For both nitrogen–decane and nitrogen–water slug flows in the microchannel, no significant dewetting of the liquid film was observed under the conditions relevant to Fig. 5a, which is reasonable given the relatively high bubble velocity involved (U_B = 49–170 mm s^{-1}) and the somewhat appreciable thickness of the liquid film around the bubble body.

In the two-phase slug flow model, the pressure drop across the body of a bubble (or a droplet) is approximated based on the viscosity of the dispersed phase (*cf.* eqn (4) or (6)). This pressure drop approximation neglects the presence of the liquid film around the bubble (or droplet) body, which is reasonable given by low capillary numbers in our experiments (Ca = 1×10^{-4}–7×10^{-3}; *cf.* Table 1) and a small percentage that thus calculated pressure drop across the bubble (or droplet) body accounts for of the measured total frictional pressure drop (well below 10% under the majority of conditions for both gas–liquid and liquid–liquid slug flows). However, at Ca typically larger than 10^{-2}, the thickness of the liquid film cannot be neglected and thus the pressure drop across the bubble (or droplet) body should be represented by further considering the velocity field and the film thickness.[27,55] As pure liquids without surfactant were used in this study, this excludes the presence of a strong Marangoni effect. The latter is likely to significantly increase the pressure drop required to drive a bubble (or a droplet) in the microchannel.[23,61] Therefore in the presence of a thick liquid film and/or a strong Marangoni effect, the pressure drop across the bubble (or droplet) body may still be approximated by eqn (4), but using an effective viscosity assumed for the dispersed phase. It should be noted that several authors reported much larger values of the effective viscosity as compared to that of the dispersed phase during droplets moving in microchannels.[62,63]

Extension of pressure drop model from a two-phase to three-phase slug flow

The above discussion corroborates the adequacy of eqn (6) in predicting the total frictional pressure drop under a two-phase slug flow provided that the wall is completely wetted by the lubricating liquid film surrounding the bubble or droplet body. Given the phenomenological resemblance between the two-phase slug flow and the nitrogen–decane–water three-phase slug flow in which the 'nitrogen-in-decane' droplet (*i.e.*, one bubble encapsulated in one decane droplet) could be considered as a pseudo-homogenous droplet (*cf.* Fig. 2a),

this equation can be extended for the estimation of the total frictional pressure drop in the three-phase slug flow. This extension is also based on the consideration that the Ca and We numbers involved in the three-phase slug flow experiments are very small as shown in Table 1, which is a necessity for the validity of eqn (6). Note that for the three-phase slug flow, $Ca = \mu_{water}U_{drop}/\sigma$ and $We = d_h U_{drop}^2 \rho_{water}/\sigma$, where σ refers to the interfacial tension for the decane–water system, ρ_{water} and μ_{water} are the density and viscosity of water, respectively, and U_{drop} is the velocity of the 'nitrogen-in-decane' droplet.

The 'nitrogen-in-decane' droplet is assumed with an effective viscosity (μ_D) expressed according to the McAdams mixture viscosity correlation as[64]

$$\mu_D = \frac{1}{x/\mu_G + (1-x)/\mu_{decane}} \quad (7)$$

where μ_G and μ_{decane} are the viscosities of nitrogen gas and decane, respectively. x is the mass fraction of gas in this pseudo-homogeneous droplet given by $x = \rho_G j_G/(\rho_G j_G + \rho_{decane} j_D)$, where ρ_G and ρ_{decane} are the densities of nitrogen gas and decane, respectively. This viscosity approximation, combined with the homogeneous flow model, has been reported to yield acceptable accuracy in estimating the pressure drop under a gas–liquid bubble flow and a slug flow in microchannels.[65,66]

Fig. 7 shows the good agreement between the measured total frictional pressure drop in the three-phase slug flow in the chip ($\Delta P_{tot,exp}$) and the model prediction ($\Delta P_{tot,model}$) given by eqn (6) in which μ_D is specified by eqn (7) and $U_S = j_G + j_D + j_W$. The predictions well describe the measurements with a standard deviation of 8%. It should be mentioned that multiple three-phase slug flow images in the middle part of microchannel segments 3–5 were measured and averaged to obtain

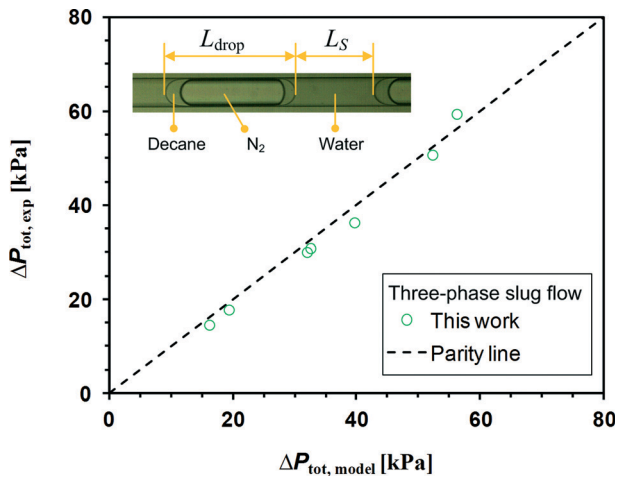

Fig. 7 The measured total frictional pressure drop ($\Delta P_{tot,exp}$) under the three-phase slug flow in the chip *versus* the model predictions ($\Delta P_{tot,model}$) given by eqn (6) and (7). The inset shows a unit cell of three-phase slug flow from which L_S and L_{drop} were obtained. The experimental data represent the area where a stable three-phase slug flow was observed throughout the current microchannel.

slug flow parameters needed in eqn (6) including L_S, L_D (= L_{drop}), and U_D (= U_{drop}) being the water slug length and the length and velocity of the 'nitrogen-in-decane' droplet, respectively (see ESI† note S2 for details about the dependence of L_S and L_{drop} on the flow conditions). An inherent precondition for this agreement is that during the three-phase slug flow experiments, there was no dewetting of the liquid film along the droplet body, which is verified by our experimental observation and can be understood based on the fact that the 'nitrogen-in-decane' droplet velocity is relatively high (U_{drop} in the range of 61.4 to 136 mm s^{-1}) and the liquid film is not very thin since the droplet travelled significantly faster than the slug (*cf.* Fig. 6a). Therefore, eqn (6) can be reliably applied for estimating the pressure drop under a three-phase slug flow in the current microchannel provided that an effective viscosity specified by eqn (7) is assumed for the 'nitrogen-in-decane' droplet.

Pressure drop under a parallel-slug flow: analogy with a two-phase parallel flow and a slug flow

The observed parallel-slug flow pattern (*cf.* Fig. 2b) features a co-flow of decane and water alongside each other with elongated nitrogen bubbles dispersed regularly in the decane phase. Intuitively, a suitable pressure drop model under this flow pattern may be obtained by combining models describing a liquid–liquid parallel flow and a slug flow in the same chip. Hereafter, we will show that this combination indeed yields satisfactory results in pressure drop estimation in the parallel-slug flow.

Interfacial position and pressure drop in a liquid–liquid parallel flow

We first investigated the decane–water parallel flow in the chip with the purpose of deriving a reasonable pressure drop model thereof. One important hydrodynamic parameter characterizing such a parallel flow is the interfacial position (β), defined as the ratio between the width of the water stream as viewed from the microchannel top surface (W_1) and the microchannel width (W), as depicted in Fig. 8a. Here, a planar decane–water interface is assumed, which thereby neglects the interface curvature induced by the interfacial tension effect (in reality, the interface would curve slightly towards the water side[67]) and facilitates our analysis. The values of β under various flow conditions were measured in the middle part of microchannel segments 3–5 and are plotted in Fig. 8b *versus* the flow ratio of water to the two-phase mixture given by $Q^* = Q_W/(Q_W + Q_D) = j_W/(j_W + j_D)$. β shows an increase with increasing Q^*. In the current experiments, β was found below around 0.5 as the flow pattern would shift to slug flow at relatively high Q^* values (*cf.* Fig. 3d). The relation between Q^* and β observed in the experiments is approximately described by the analytical equation derived by Hitt and Macken[68] for describing the planar surface position formed between converging flows of two substreams of one identical liquid in a

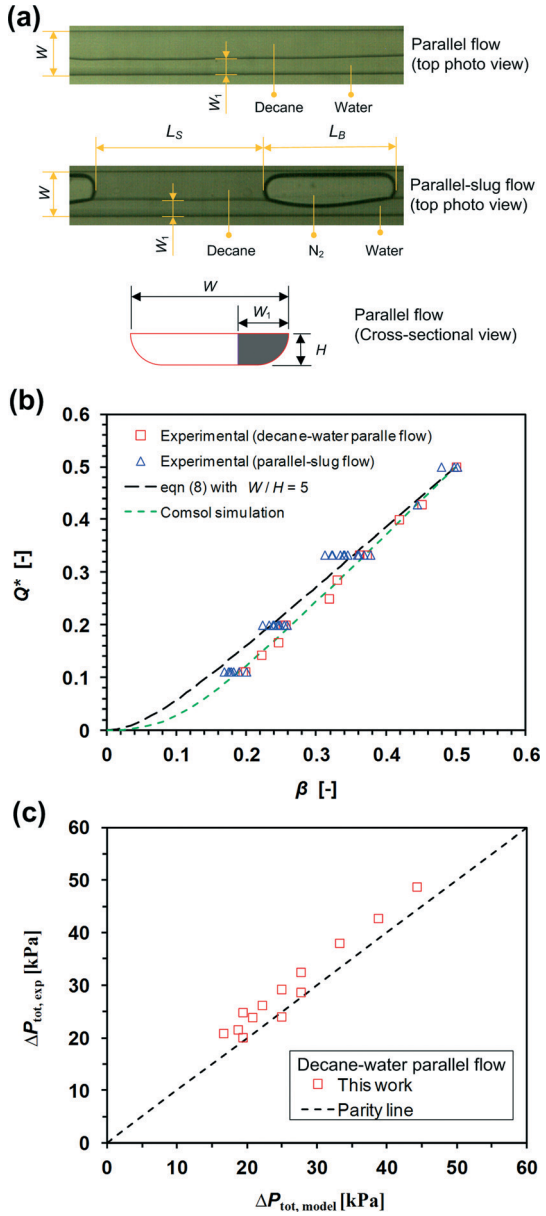

Fig. 8 (a) Images showing how to measure the interfacial position ($\beta = W_1/W$) in the decane–water parallel flow pattern and the nitrogen–decane–water parallel-slug flow pattern. The definition of L_S and L_B is also shown in the image for the parallel-slug flow pattern. The bottom schematic shows a cross-sectional view of the assumed planar decane–water interface in the parallel flow pattern. The area to the right of the interface is occupied by water (shadowed) and the area to the left is occupied by decane. (b) The measured Q^* as a function of β for the decane–water parallel flow pattern and the nitrogen–decane–water parallel-slug flow pattern. The experimental results are also compared with the prediction made with eqn (8) and Comsol simulations (see ESI† note S3). The experimental data for the parallel flow pattern were collected under j_D = 25.3–40.5 mm s^{-1} and j_W = 3.8–40.5 mm s^{-1}. The experimental data for the parallel-slug flow pattern were collected under $j_{G,STP}$ = 30.4–91.2 mm s^{-1}, j_D = 10.1–40.5 mm s^{-1}, and j_W = 2.5–40.5 mm s^{-1}. (c) Parity plot for the prediction made with eqn (9) and the measured total frictional pressure drop under the decane–water parallel flow.

rectangular microchannel (at W/H = 5) under fully-developed laminar flow conditions, that is,

$$Q^* = \frac{\frac{\beta W}{3H} - \frac{32}{\pi^5}\sum_{n=0}^{\infty}\frac{\tanh\left((n+1/2)\pi W/H\right)}{(2n+1)^5}}{\frac{W}{3H} - \frac{64}{\pi^5}\sum_{n=0}^{\infty}\frac{\tanh\left((n+1/2)\pi W/H\right)}{(2n+1)^5}} + \frac{\frac{32}{\pi^5}\sum_{n=0}^{\infty}\frac{\sinh\left((n+1/2)(1-2\beta)\pi W/H\right)}{(2n+1)^5\cosh\left((n+1/2)\pi W/H\right)}}{\frac{W}{3H} - \frac{64}{\pi^5}\sum_{n=0}^{\infty}\frac{\tanh\left((n+1/2)\pi W/H\right)}{(2n+1)^5}} \quad (8)$$

This agreement indicates that the present microchannel shape can be approximated as rectangular and one more important implication is that the decane–water parallel flow could be possibly considered as the co-flow of one identical fluid, which is supported by the fact that the viscosity of decane (μ_{decane} = 0.92 mPa s) is very close to that of water (μ_{water} = 1 mPa s) under the experimental conditions. Therefore, the combined velocity profile of both phases would resemble much a fully-developed laminar flow that one identical fluid experiences when flowing alone in the microchannel at the total flow rate of the mixture. This implication is further justified as can be seen from Fig. 8b that the measured β fits even better with the prediction given by our Comsol simulation of a single-phase water flow in the chip from which Q^* can be derived for a given β since the laminar velocity profile over the microchannel cross section is known by simulation (as shown in ESI† note S3).

Based on these observations, the pressure drop under the decane–water parallel flow is approximately equal to that caused by a single-phase laminar flow of water in the same microchannel at a flow rate equal to the total flow rate of the two phases, which yields

$$\Delta P_{tot} = \frac{C\mu_{water}L(j_D + j_W)}{2d_h^2} \quad (9)$$

This assumption is verified in Fig. 8c which shows that the measured total frictional pressure drop under the decane–water parallel flow in the microchannel ($\Delta P_{tot,exp}$) agrees favorably with the prediction of eqn (9) ($\Delta P_{tot,model}$). An overall slight underestimation in the prediction can be explained primarily by the fact that eqn (9) treats the two phases as one identical fluid of water and thus does not consider the viscosity difference between them which can to some extent cause a deviation in the velocity profile of each phase from a fully-developed one when each phase is assumed to flow alone in the microchannel.[67] This velocity deviation translates into a slightly higher pressure gradient along the microchannel wall. It may be mentioned that a water-only instead of a decane-only flow is assumed here given the slight higher viscosity of water which partly offsets such underestimation.

Combination of models in a two-phase slug flow and a parallel flow for use in three-phase parallel-slug flow

We then studied the interfacial position under the nitrogen–decane–water parallel-slug flow in the chip. As also shown in Fig. 8a, the same planar liquid–liquid interface could be assumed in this flow pattern especially for the region where the decane slug meets the adjacent water stream. In the region containing bubbles, a temporarily curved decane–water interface was observed as the bubble could expand towards the water side (as also shown in ESI† movie S7). We measured the decane–water interfacial position ($\beta = W_1/W$) from the captured parallel-slug flow images in the middle part of microchannel segments 3–5. Fig. 8b reveals that like in the case of the decane–water parallel flow, the relation between the measured β and Q^* in the parallel-slug flow pattern could be roughly described by eqn (8) and the prediction according to our Comsol simulation results on the single-phase laminar flow of water in the chip (as shown in ESI† note S3). This suggests that the presence of bubbles in an otherwise decane–water parallel flow does not modify the interfacial position between the two liquid phases and thus the flow in the region where the decane slug travels alongside with the water stream could also be approximately described as the laminar flow of one identical fluid (*e.g.*, water), as discussed above. According to the mass balance for the nitrogen and decane phases, the decane slug has an average velocity of $U_S = (j_G + j_D)/(1 - R_1)$. Here R_1 is the ratio of the cross-sectional area occupied by water to the microchannel cross-sectional area (see the cross-sectional view shown in 8a) and can be determined for a given β to be

$$R_1 = \frac{\arccos\left(1-\beta\frac{W}{H}\right)-\left(1-\beta\frac{W}{H}\right)\sqrt{2\beta\frac{W}{H}-\left(\beta\frac{W}{H}\right)^2}}{\pi-4+2W/H} \quad (10)$$

at $\beta < H/W$ and

$$R_1 = \frac{1}{2} - \frac{1-2\beta}{2+(\pi-4)H/W} \quad (11)$$

at $H/W \le \beta \le 1/2$.

Fig. 9a shows that the decane slug moved slightly slower than the nitrogen bubble (the velocity being U_B) due to the presence of a decane film around the bubble. The average velocity of the water stream (U_W) in contact with the decane slug can be estimated as $U_W = (j_G + j_D)j_W/(j_D R_1)$. This estimation is based on the consideration that the U_W/U_S ratio in this region under parallel-slug flow should be the same as the ratio between the average velocities of the co-flowing water and decane streams within a parallel flow ($= j_W(1 - R_1)/(j_D R_1)$), given the same interfacial position for a fixed set of j_D and j_W (Fig. 8b) and the approximation of parallel flow by the laminar flow of one identical fluid in both cases. Obviously, in this region U_W is larger than j_W/R_1 (a value equal to the average velocity of the water stream if it is assumed to move at a constant speed within a parallel-slug flow). This indicates that the water stream actually did not move at a constant speed,

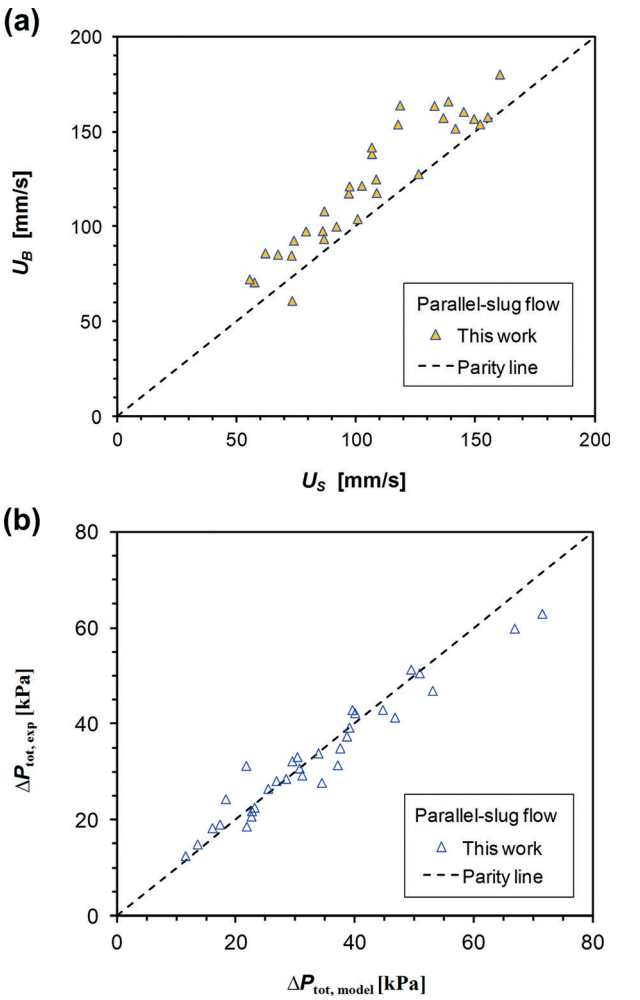

Fig. 9 (a) Bubble velocity (U_B) as a function of the average velocity in the decane slug (U_S) under the parallel-slug flow observed in the chip. (b) Parity plot for the prediction made with eqn (12) and the measured total frictional pressure drop under the parallel-slug flow.

which is true as in the region where water travelled alongside with the bubble, the local average velocity of the water stream should be significantly lower than j_W/R_1 from a pressure balance point of view. In other words, the pressure drop along the bubble body and that experienced in water should be the same. However, given the much higher viscosity of water as compared to that of nitrogen, the velocity magnitude in water is very small in this region. Therefore, one important finding here is that although the presence of bubbles in an otherwise decane–water parallel flow did not change the interfacial position, it induced a significant change in the flow field of the co-flowing water stream which was accelerated when water approached the decane slug and was decelerated when water approached the bubble body.

Now we can formulate an approximate pressure drop model for parallel-slug flow by considering that the total frictional pressure drop (ΔP_{tot}) in this flow pattern consists of the contributions from: (i) the pressure drop in the region where the decane slug meets the water stream (ΔP_S), which could be

approximated as the laminar pressure drop caused by the water-only flow in the microchannel at an average velocity being $U_{avg} = U_S(1 - R_1) + U_W R_1 = (j_G + j_D)(1 + j_W/j_D)$; (ii) the pressure drop in the region where the water stream travels alongside with the bubble, which could be assumed as the sum of the pressure drop across the bubble end caps (ΔP_{caps}) and that across the bubble body (ΔP_{body}); here the same pressure gradient is assumed to exist in each phase.

The process of model development in the two-phase slug flow (see eqn (1)–(6)) can be reproduced here, since both Ca and We numbers involved are also roughly much smaller than 1 (Table 1). It should be mentioned that Ca and We numbers under parallel-slug flow are calculated using the properties relevant to the local nitrogen–decane slug flow within this flow pattern (Ca = $\mu_{decane} U_B/\sigma$, We = $d_h U_B^2 \rho_{decane}/\sigma$; where σ refers to the surface tension for the nitrogen–decane system). Therefore the total frictional pressure drop in parallel-slug flow can be represented by

$$\Delta P_{tot} = \Delta P_S + \Delta P_{body} + \Delta P_{caps} = \frac{nC\mu_{water} L_S (j_G + j_D)(1 + j_W/j_D)}{2d_h^2} + \frac{nC\mu_G L_{body} U_B}{2d_e^2} + c_1 \frac{n\mathrm{Ca}^{2/3}\sigma}{H} \quad (12)$$

where $C = 75.33$ and $c_1 = 16$ for the present microchannel geometry, Ca = $\mu_{decane} U_B/\sigma$, $n = L/(L_B + L_S)$, and $L_{body} \approx L_B - d_e$ (see ESI† note S2 for more information on L_B and L_S). Here d_e denotes the effective hydraulic diameter for the bubble moving in the decane phase and can be taken as $d_e = d_h$ as a first approximation. This is based on the following considerations: first, d_e derived based on the cross-sectional area that the nitrogen and decane phases occupied under the investigated conditions (*i.e.*, $\beta \leq 0.5$, $R_1 \leq 0.5$) is very close to d_h (as shown in ESI† note S4). Second, ΔP_{body} is not the dominant contribution here since the calculated ΔP_{body} with $d_e = d_h$, that is, $\Delta P_{body} = nC\mu_G L_{body} U_B/(2d_e^2)$, is below 6% of the measured total frictional pressure drop under the current conditions, which relaxes the choice of a precise value for d_e. Fig. 9b shows that the measured total frictional pressure drop ($\Delta P_{tot,exp}$) under parallel-slug flow in the microchannel compares fairly well with the model prediction ($\Delta P_{tot,model}$) given by eqn (12), where a standard deviation of only 12% was found in the prediction.

Application of the pressure drop model for the design of bifurcated microchannels to split a three-phase slug flow for high-throughput processing

The developed pressure drop models can be used to estimate three-phase hydrodynamic resistance in microfluidic systems. Here we illustrate the approach in the design of bifurcated microchannels to split a three-phase slug flow. A network of 3-level microchannels etched in glass is considered (Fig. 10a), where a nitrogen–decane–water three-phase slug flow from a single microchannel at level 1 is evenly split into two identical microchannels at level 2, followed by another flow splitting into four microchannels at level 3. This example represents a possible way to increase the production rate under three-phase flow processing, as already shown for the production of oil-in-water-in-oil (O/W/O) double emulsions.[69]

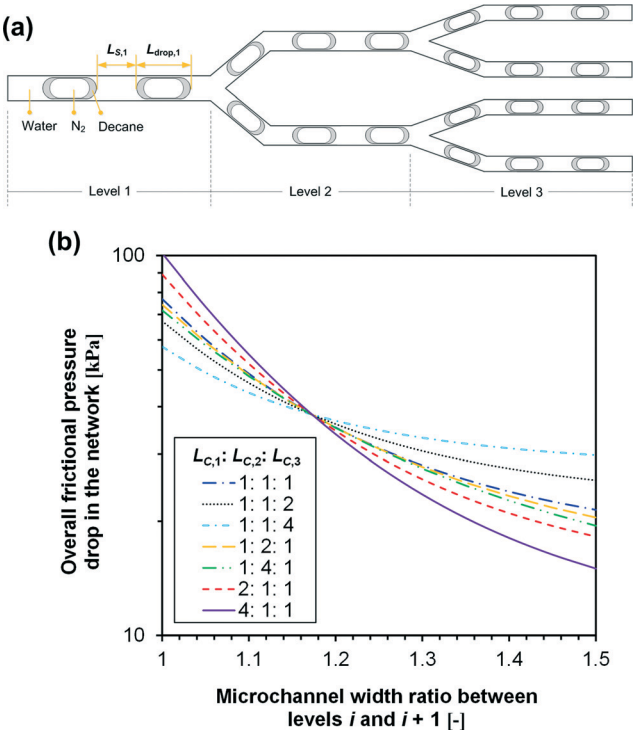

Fig. 10 (a) Schematic illustration of a 3-level microchannel network for evenly splitting a nitrogen–decane–water three-phase slug flow. The local splitting of the 'nitrogen-in-decane' droplet at each bifurcation is not shown. (b) The overall frictional pressure drop during the three-phase slug flow in the network ($\Delta P_{tot,C}$) as a function of the microchannel width ratio between levels i and i + 1 ($W_{C,i}/W_{C,i+1}$). Data are shown for a given condition at $j_{G,3}$ = 25.8 mm s^{-1}, $j_{D,3}$ = 7.6 mm s^{-1}, $j_{W,3}$ = 30.4 mm s^{-1}, $H_{C,3}$ = 60 μm; $W_{C,3}$ = 300 μm, $L_{S,3}/W_{C,3}$ = 3.8, $L_{drop,3}/W_{C,3}$ = 5.3. The total length of the network (= $L_{C,1}$ + $L_{C,2}$ + $L_{C,3}$) is fixed at 150 mm.

The exact value of hydrodynamic resistance in this network is necessary for a suitable design of microchannel geometries thereof. The cross-sectional shape of all microchannels in the network is assumed to be the same as used in our experiments ($H_{C,i}$, $W_{C,i}$, $L_{C,i}$, $A_{C,i}$ and $d_{h,i}$ being the height, top width, length, cross-sectional area and hydraulic diameter of one microchannel at level i respectively; i = 1, 2, 3). Then, the total frictional pressure drop during three-phase slug flow in each microchannel at level i ($\Delta P_{tot,i}$) can be represented according to eqn (6) as

$$\Delta P_{tot,i} = \frac{L_{C,i}}{L_{S,i} + L_{drop,i}} \left[\frac{c_1 \mathrm{Ca}_i^{2/3}\sigma}{H_{C,i}} + \frac{C\mu_C L_{S,i} U_{S,i}}{2d_{h,i}^2} + \frac{C\mu_{D,i}(L_{drop,i} - d_{h,i}) U_{drop,i}}{2d_{h,i}^2} \right] \quad (13)$$

where subscript i at the corresponding symbols ($U_{s,i}$, $L_{s,i}$, $U_{drop,i}$, $L_{drop,i}$, Ca_i, $\mu_{D,i}$) shows the level index. Ca_i (= $\mu_{water} U_{drop,i}/\sigma$) is the capillary number at level i. $\mu_{D,i}$ is calculated using eqn (7) with $x = \rho_G j_{G,i}/(\rho_G j_{G,i} + \rho_{decane} j_{D,i})$. The superficial velocities

at level i for nitrogen, decane and water are denoted as $j_{G,i}$, $j_{D,i}$ and $j_{W,i}$, respectively. The ratio of superficial velocities between levels i and $i + 1$ for each phase (*e.g.*, $j_{G,i}/j_{G,i+1}$) is equal to $2A_{i+1}/A_i$ according to the conservation of mass. It is also assumed that the 'nitrogen-in-decane' droplets, including their body and end caps, occupy the entire cross section of the microchannel at each level. In other words, there is no communication between two adjacent liquid slugs. In this case, the following relations can be derived for a first approximation: $L_{S,i}/L_{S,i+1} = L_{drop,i}/L_{drop,i+1} = 2A_{i+1}/A_i$ and $U_{S,i} = U_{D,i} = j_{G,i} + j_{D,i} + j_{W,i}$.

Fig. 10b shows the overall frictional pressure drop during the three-phase slug flow in the network, $\Delta P_{tot,C}$ (= $\Delta P_{tot,1}$ + $\Delta P_{tot,2}$ + $\Delta P_{tot,3}$), as a function of the geometrical parameters of the network at a given set of conditions similar to those in our experiments ($j_{G,3}$ = 25.8 mm s^{-1}, $j_{D,3}$ = 7.6 mm s^{-1}, $j_{W,3}$ = 30.4 mm s^{-1}, $H_{C,3}$ = 60 μm; $W_{C,3}$ = 300 μm, $L_{S,3}/W_{C,3}$ = 3.8, $L_{drop,3}/W_{C,3}$ = 5.3). The total length of the network (= $L_{C,1}$ + $L_{C,2}$ + $L_{C,3}$) is arbitrarily fixed at 150 mm.

As expected, $\Delta P_{tot,C}$ decreases with increasing the microchannel width ratio between levels i and $i + 1$ (*i.e.*, $W_{C,i}/W_{C,i+1}$; = $H_{C,i}/H_{C,i+1}$). $\Delta P_{tot,C}$ also depends on the microchannel length at each level. Under the chosen conditions, $\Delta P_{tot,C}$ can be lowered by increasing the microchannel length at level 3 at $W_{C,i}/W_{C,i+1} < 1.17$ or by increasing the microchannel length at level 1 at $W_{C,i}/W_{C,i+1} > 1.17$. This result can be explained by the difference in the relative contribution of $\Delta P_{tot,i}$ towards the overall $\Delta P_{tot,C}$: at the first level (i = 1), $\Delta P_{tot,i}$ could be higher than that at the third level (i = 3) due to the much higher droplet velocity at level 1 when $W_{C,i}/W_{C,i+1}$ is not large enough.

This example shows the importance of the pressure drop calculation in providing useful guidelines in a microfluidic system design prior to their fabrication. In several cases, *viz.* extraction or chemical reaction under three-phase flow, additional constrains related to the residence time and/or the minimum (or maximum) channel depth related to microfabrication methods can be present. Such constraints can be incorporated into the pressure drop models to obtain an optimal design of the system. For the microchannel network shown in Fig. 10a, uneven flow splitting or even no splitting of droplets could occur at several bifurcation points. The performance of the network depends on the three-phase flow pattern, channel dimensions and fluid properties.[69] In this case, the corresponding pressure drop model can be applied to understand the path selection behavior of droplets or bubbles in the network, thereby providing the direction for improvement.

Conclusion

We have experimentally studied the nitrogen–decane–water flow in a glass microfluidic chip which comprises a serpentine microchannel (the hydraulic diameter being 98 μm) fed with a cross-flow mixer. Two major flow patterns were identified as three-phase slug flow and parallel-slug flow. The three-phase slug flow pattern is characterized by an alternate flow of water slugs and decane droplets containing single elongated nitrogen bubbles. This regime can be seen as a superimposition of both decane–water and nitrogen–decane slug flows that were observed in the same chip when the flow of the third phase (*viz.* nitrogen or water, respectively) was set at zero. It was observed at a superficial velocity of decane (in the range of about 0.6 to 10 mm s^{-1}) typically lower than that of water for a given superficial gas velocity in the range of 30 to 91 mm s^{-1}. The parallel-slug flow pattern is characterized by a side-by-side flow of water with respect to the decane carrying dispersed nitrogen bubbles. The latter regime can be seen as a superimposition of the decane–water parallel flow and the nitrogen–decane slug flow present in the chip under the corresponding two-phase flow conditions, which was observed at a superficial velocity of decane (in the range of about 2.5 to 40 mm s^{-1}) typically higher than that of water for each given superficial gas velocity.

Two pressure drop models for the three-phase slug flow and parallel-slug flow were developed based on the combination and/or extension of the two-phase (slug flow and parallel flow) pressure drop models. The three-phase slug flow model as specified in eqn (6) and (7) takes into account the pressure drop contributions from water slugs, the body and end caps of the pseudo-homogeneous 'nitrogen-in-decane' droplets. The parallel-slug flow model as specified in eqn (12) takes into account the pressure drop in the region with the local decane–water parallel flow plus the pressure drop caused by nitrogen bubbles moving in the decane phase. The developed models can be further extrapolated for other microchannel geometries under the condition of small capillary and Weber numbers (Ca $\ll$ 0.1, We $\ll$ 1) provided that the laminar friction constant (C) and the geometrical parameter (c_1) thereof are known. In case of a large difference in viscosity between the two liquid phases, the parallel-slug flow model has to be modified, by reconsidering the pressure drop in the region where the two liquid streams align each other (*i.e.*, ΔP_S in eqn (12)).

The findings of this work open up new opportunities for chemists and engineers who want to better control gas–liquid–liquid operations in microfluidic systems, among other in multiphase catalysis, materials synthesis and liquid–liquid extraction. The proposed pressure drop models can be used to predict the bubble/droplet trafficking in bifurcated microchannels under three-phase flow processing. These models can also be applied to design on-chip pressure barrier channels that introduce a large pressure drop in the feeding side of each phase in order to dampen unwanted fluctuations in a three-phase flow.[70]

Acknowledgements

This work was carried out in close cooperation with Chemtrix B.V. and is financially supported by SenterNovem and Pieken in de Delta (PID project 'Modular MRT platform', no. PID081014). The authors wish to sincerely thank them for their support.

Notes and references

1 A. Günther and K. F. Jensen, *Lab Chip*, 2006, **6**, 1487–1503.
2 K. Jähnisch, V. Hessel, H. Löwe and M. Baerns, *Angew. Chem., Int. Ed.*, 2004, **43**, 406–446.
3 B. P. Mason, K. E. Price, J. L. Steinbacher, A. R. Bogdan and D. T. McQuade, *Chem. Rev.*, 2007, **107**, 2300–2318.
4 C. Wiles and P. Watts, *Chem. Commun.*, 2011, **47**, 6512–6535.
5 S. Marre and K. F. Jensen, *Chem. Soc. Rev.*, 2010, **39**, 1183–1202.
6 A. Abou-Hassan, O. Sandre and V. Cabuil, *Angew. Chem., Int. Ed.*, 2010, **49**, 6268–6286.
7 R. L. Hartman, H. R. Sahoo, B. C. Yen and K. F. Jensen, *Lab Chip*, 2009, **9**, 1843–1849.
8 O. K. Castell, C. J. Allender and D. A. Barrow, *Lab Chip*, 2009, **9**, 388–396.
9 S. Hardt and T. Hahn, *Lab Chip*, 2012, **12**, 434–442.
10 N. Assmann, A. Ładosz and P. R. von Rohr, *Chem. Eng. Technol.*, 2013, **36**, 921–936.
11 J. Atencia and D. J. Beebe, *Nature*, 2005, **437**, 648–655.
12 H. Song, D. L. Chen and R. F. Ismagilov, *Angew. Chem., Int. Ed.*, 2006, **45**, 7336–7356.
13 L. Shui, J. C. T. Eijkel and A. van den Berg, *Adv. Colloid Interface Sci.*, 2007, **133**, 35–49.
14 M. L. Kovarik, P. C. Gach, D. M. Ornoff, Y. Wang, J. Balowski, L. Farrag and N. L. Allbritton, *Anal. Chem.*, 2012, **84**, 516–540.
15 J. Yue, G. Chen, Q. Yuan, L. Luo and Y. Gonthier, *Chem. Eng. Sci.*, 2007, **62**, 2096–2108.
16 M. N. Kashid, A. Renken and L. Kiwi-Minsker, *Chem. Eng. Sci.*, 2011, **66**, 3876–3897.
17 R. Dreyfus, P. Tabeling and H. Willaime, *Phys. Rev. Lett.*, 2003, **90**, 144505.
18 J. Yue, L. Luo, Y. Gonthier, G. Chen and Q. Yuan, *Chem. Eng. Sci.*, 2008, **63**, 4189–4202.
19 N. Shao, A. Gavriilidis and P. Angeli, *Chem. Eng. Sci.*, 2009, **64**, 2749–2761.
20 C.-X. Zhao and A. P. J. Middelberg, *Chem. Eng. Sci.*, 2011, **66**, 1394–1411.
21 T. Cubaud and C.-M. Ho, *Phys. Fluids*, 2004, **16**, 4575–4585.
22 A. Salim, M. Fourar, J. Pironon and J. Sausse, *Can. J. Chem. Eng.*, 2008, **86**, 978–988.
23 M. J. Fuerstman, A. Lai, M. E. Thurlow, S. S. Shevkoplyas, H. A. Stone and G. M. Whitesides, *Lab Chip*, 2007, **7**, 1479–1489.
24 J. Yue, L. Luo, Y. Gonthier, G. Chen and Q. Yuan, *Chem. Eng. Sci.*, 2009, **64**, 3697–3708.
25 S. A. Vanapalli, A. G. Banpurkar, D. van den Ende, M. H. G. Duits and F. Mugele, *Lab Chip*, 2009, **9**, 982–990.
26 S. Molla, D. Eskin and F. Mostowfi, *Lab Chip*, 2011, **11**, 1968–1978.
27 J. Jovanović, W. Zhou, E. V. Rebrov, T. A. Nijhuis, V. Hessel and J. C. Schouten, *Chem. Eng. Sci.*, 2011, **66**, 42–54.
28 P. Garstecki, M. J. Fuerstman, H. A. Stone and G. M. Whitesides, *Lab Chip*, 2006, **6**, 437–446.
29 A. R. Abate, P. Mary, V. van Steijn and D. A. Weitz, *Lab Chip*, 2012, **12**, 1516–1521.
30 D. M. Fries, F. Trachsel and P. R. von Rohr, *Int. J. Multiphase Flow*, 2008, **34**, 1108–1118.
31 C. N. Baroud, F. Gallaire and R. Dangla, *Lab Chip*, 2010, **10**, 2032–2045.
32 P. Parthiban and S. A. Khan, *Lab Chip*, 2012, **12**, 582–588.
33 Y. Önal, M. Lucas and P. Claus, *Chem. Eng. Technol.*, 2005, **28**, 972–978.
34 B. Zheng and R. F. Ismagilov, *Angew. Chem., Int. Ed.*, 2005, **44**, 2520–2523.
35 N. Aoki, R. Ando and K. Mae, *Ind. Eng. Chem. Res.*, 2011, **50**, 4672–4677.
36 N. Assmann and P. R. von Rohr, *Chem. Eng. Process.*, 2011, **50**, 822–827.
37 Y. Su, G. Chen, Y. Zhao and Q. Yuan, *AIChE J.*, 2009, **55**, 1948–1958.
38 M. Hashimoto, P. Garstecki and G. M. Whitesides, *Small*, 2007, **3**, 1792–1802.
39 S. Khan and S. Duraiswamy, *Lab Chip*, 2009, **9**, 1840–1842.
40 A. R. Abate and D. A. Weitz, *Lab Chip*, 2011, **11**, 1713–1716.
41 J. Wan, A. Bick, M. Sullivan and H. A. Stone, *Adv. Mater.*, 2008, **20**, 3314–3318.
42 M. H. Lee, V. Prasad and D. Lee, *Langmuir*, 2010, **26**, 2227–2230.
43 J. H. Xu, R. Chen, Y.-D. Wang and G. S. Luo, *Lab Chip*, 2012, **12**, 2029–2036.
44 J. Wan and H. A. Stone, *Langmuir*, 2012, **28**, 37–41.
45 V. M. Rajesh and V. V. Buwa, *Chem. Eng. J.*, 2012, **207–208**, 832–844.
46 K. Wang, Y. C. Lu, J. Tan, B. D. Yang and G. S. Luo, *Microfluid. Nanofluid.*, 2010, **8**, 813–821.
47 K. Wang, Y. Lu, K. Qin, G. Luo and T. Wang, *Chem. Eng. Technol.*, 2013, **36**, 1047–1060.
48 B. M. A. Wolffenbuttel, T. A. Nijhuis, A. Stankiewicz and J. A. Moulijn, *Meas. Sci. Technol.*, 2002, **13**, 1540–1544.
49 P. Guillot and A. Colin, *Phys. Rev. E: Stat., Nonlinear, Soft Matter Phys*, 2005, **72**, 066301.
50 R. T. Baker and W. Tumas, *Science*, 1999, **284**, 1477–1479.
51 G. Tanarungsun, H. Yamada, T. Tagawa, W. Kiatkittipong, P. Praserthdam and S. Assabumrungrat, *Chem. Eng. Process.*, 2011, **50**, 53–58.
52 T. Rahman, P. G. Krishnamurthy, P. Parthiban, A. Jain, C. P. Park, D.-P. Kim and S. A. Khan, *RSC Adv.*, 2013, **3**, 2897–2900.
53 H. Wong, C. J. Radke and S. Morris, *J. Fluid Mech.*, 1995, **292**, 95–110.
54 S. R. Hodges, O. E. Jensen and J. M. Rallison, *J. Fluid Mech.*, 2004, **501**, 279–301.
55 R. Gupta, S. S. Y. Leung, R. Manica, D. F. Fletcher and B. S. Haynes, *Chem. Eng. Sci.*, 2013, **92**, 180–189.
56 C. Redon, F. Brochard-Wyart and F. Rondelez, *Phys. Rev. Lett.*, 1991, **66**, 715–718.
57 C. Y. Lee and S. Y. Lee, *Exp. Therm. Fluid Sci.*, 2010, **34**, 1–9.
58 K. R. Shull and T. E. Karis, *Langmuir*, 1994, **10**, 334–339.
59 H. Haidara, L. Vonna and J. Schultz, *Langmuir*, 1998, **14**, 3425–3434.
60 N. Péron, F. Brochard-Wyart and H. Duval, *Langmuir*, 2012, **28**, 15844–15852.
61 K. J. Stebe, S. Y. Lin and C. Maldarelli, *Phys. Fluids A*, 1991, **3**, 3–20.

62 L. Salkin, L. Courbin and P. Panizza, *Phys. Rev. E: Stat., Nonlinear, Soft Matter Phys*, 2012, **86**, 036317.
63 L. Salkin, A. Schmit, L. Courbin and P. Panizza, *Lab Chip*, 2013, **13**, 3022–3032.
64 W. H. McAdams, *Heat Transmission*, McGraw-Hill, New York, 3rd edn, 1954.
65 K. A. Triplett, S. M. Ghiaasiaan, S. I. Abdel-Khalik, A. LeMouel and B. N. McCord, *Int. J. Multiphase Flow*, 1999, **25**, 395–410.
66 J. Yue, G. Chen and Q. Yuan, *Chem. Eng. J.*, 2004, **102**, 11–24.
67 A. Pohar, M. Lakner and I. Plazl, *Microfluid. Nanofluid.*, 2012, **12**, 307–316.
68 D. L. Hitt and N. Macken, *J. Fluids Eng.*, 2004, **126**, 758–767.
69 A. R. Abate and D. A. Weitz, *Lab Chip*, 2011, **11**, 1911–1915.
70 M. Al-Rawashdeh, F. Yu, T. A. Nijhuis, E. V. Rebrov, V. Hessel and J. C. Schouten, *Chem. Eng. J.*, 2012, **207–208**, 645–655.